Selection for targeted therapy resistance leads to an indirect selection for higher phenotypic plasticity and enhanced evolvability to orthogonal stressors

Alicia Bjornberg[1,2*], Aobuli Xieraili[1*], Matthew Froid[2,3], Rowan Barker-Clarke[4], Jeff Maltas[4], Robert Vander Velde[5], Jamir Riffas[2], Berkley Gryder[6], Jacob Scott[4], David Bassanta[3], Alexander RA Anderson[3], Virginia A Turati[3,7+], Andriy Marusyk[1+]

1. Department of Tumor Microenvironment and Metastasis, H Lee Moffitt Cancer Center and Research Institute, Tampa, FL, USA
2. Department of Molecular Biosciences, University of South Florida, Tampa, FL, USA
3. Department of Integrated Mathematical Oncology, H Lee Moffitt Cancer Center and Research Institute, Tampa, FL, USA
4. Department of Translational Hematology and Oncology Research, Cleveland Clinic, Cleveland, OH, USA
5. Department of Bioengineering, School of Engineering and Applied Sciences, University of Pennsylvania, Philadelphia, PA, USA
6. Department of Genetics and Genome Sciences, Case Western Reserve University, Cleveland, OH, USA
7. Division of Molecular Medicine and Gene Therapy, Lund University, Lund, SE

*, + Equal contribution

Corresponding Author Contact: andriy.marusyk@moffitt.org

ABSTRACT

Acquired resistance to targeted therapies is the primary barrier to durable cancer remission. Therapy resistance is often associated with stemness and intermediate EMT programs, which are often viewed as proximal resistance mechanisms. On the other hand, a growing body of evidence suggests that these programs facilitate resistance through plasticity-mediated adaptations. Integrating computational modeling, functional experimental assays, and lineage tracing, we investigated the relationship between EMT and therapy resistance in experimental models of acquired resistance to ALK+ lung cancer. Our results support a model where phenotypic plasticity, associated with intermediate EMT, is a selectable trait, and selection for subpopulations with higher phenotypic plasticity is amplified under a multifactorial resistance scenario. Consequently, resistance to targeted therapy is associated with higher ability to adapt to orthogonal therapeutic and environmental stressors, as well as higher metastatic potential. These findings identify cellular plasticity as the fundamental substrate from which multifactorial resistance and metastatic competence evolve, indicating that

targeting phenotypic plasticity can suppress the acquisition of resistance and prolong therapeutic responses.

INTRODUCTION

Targeted therapies, particularly small-molecule inhibitors designed to exploit oncogenic signaling dependencies, have transformed the treatment landscape for advanced cancers[1–3]. In subsets of patients, these agents induce profound and durable initial responses. However, in most cases, targeted therapies fail to eliminate the disease, and the residual populations eventually develop resistance, leading to cancer relapse[4]. The inevitability of acquired resistance limits the lasting benefit of targeted therapy, making it imperative to elucidate the fundamental principles governing its emergence and evolution.

Therapy resistance is commonly attributed to a single or dominant mechanism, including mutational or expression level changes[5]. However, our studies on the evolution of resistance to pharmacological inhibitors of EML4-Alk fusion (ALKi) in non–small cell lung cancer (NSCLC) have suggested a more complex scenario of multifactorial resistance. Specifically, we demonstrated that resistance to distinct ALKi can emerge from the accumulation of multiple genetic and non-genetic adaptations within the same cells[6]; similar observations were reported in other contexts of acquired therapy resistance[7,8]. Whereas exposure to pharmacologically distinct ALK inhibitors (ALKi) resulted in predictably distinct combinations of resistance mechanisms, we noticed that resistant cells shared epithelial-to-mesenchymal (EMT)- and stemness-associated programs.

Intermediate EMT, which is associated with enhanced stemness[9,10], is linked with therapy resistance across multiple therapeutic contexts, including resistance to targeted therapies in NSCLC[9,11–13]. This link is often attributed to stemness and EMT representing proximal (direct) resistance mechanisms, analogous to resistance-conferring mutations or elevated expression of genes that activate bypass signaling mechanisms[14,15]. However, experimental activation of EMT was insufficient to confer ALKi resistance[6]. On the other hand, we found that ALKi-resistant cells displayed an enhanced potential to develop resistance to orthogonal pharmacological and environmental stressors, including enhanced metastatic potential.

To dissect the relationship between plasticity and adaptive capacity, we employed a combination of *in silico* modeling, and molecular and functional interrogation of NSCLC subpopulations with varying ability to develop ALKi resistance. Our studies suggest a model in which therapy-naïve cancers contain subpopulations with varying ability to adapt to targeted therapies, where higher adaptive potential is associated with enhanced phenotypic plasticity, characterized by an enrichment of EMT- and stemness-

associated transcription factor networks, including KLF4 and SOX family members. The multifactorial nature of targeted therapy resistance leads to progressive enrichment of subpopulations with higher plasticity, as these subpopulations are more likely to undergo adaptive cell state transitions, eventually culminating in strong therapy resistance. Subpopulations with low adaptive potential can be converted into high adaptive potential by expression of Yamanaka factors[16] or the EMT regulator Slug. Conversely, high adaptive potential can be blocked by the genetic knockdown of stemness-associated transcriptional factors or the use of pharmacological inhibitors of epigenetic reprogramming. Our studies suggest that suppressing phenotypic plasticity can enhance long-term responses to targeted therapies, thereby limiting the emergence of resistance.

RESULTS

ALK inhibitor resistance is associated with EMT, stemness, and broad adaptive capacity

Our previous work showed that the development of resistance in ALK-rearranged NSCLC is characterized by the gradual accumulation of genetic and epigenetic changes, with each tyrosine kinase inhibitor (TKI) giving rise to distinct, reproducible transcriptional phenotypes[7]. Building on this, we asked whether, despite their divergent trajectories, there are shared features that emerge across independently evolved resistance states. To generate resistant derivatives for these analyses, treatment-naïve parental H3122 cells were continuously exposed to ALKi until stably resistant, yielding lorlatinib-evolved (erLor) or alectinib-evolved (erAlec) resistant cells (collectively erALKi) (**Fig. 1A**)[6]. Our immediate goal was to identify transcriptional programs that recur across drug-specific resistance states and capture the combined impact of genetic alterations and adaptive gene expression changes, rather than a single, drug-specific mechanism. These evolved resistant cells displayed a mesenchymal morphology distinct from treatment-naïve counterparts (**Fig. 1B**). In both erALKi populations, transcriptomic profiling and gene set enrichment analysis (GSEA) demonstrated activation of tumor necrosis factor-alpha (TNF-α) and transforming growth factor-beta (TGF-β) signaling pathways (**Fig. 1C-D, Fig. S1A-B**), both previously implicated in EMT, stemness, and metastatic potential[17–23]. Since EMT regulates programs beyond drug tolerance, including stemness and adaptation to microenvironmental stress, and because adaptation to distinct ALKi converges on EMT-associated pathways, we hypothesized that EMT does not function primarily as a direct mechanism of drug escape. Rather, it might reflect it might reflect a more plastic cell state that enhances cellular evolvability, thereby providing a substrate from which diverse routes of therapy resistance can be selected under pressure.

To test this hypothesis, we quantified transcriptional entropy using the Gini index, a metric previously applied to infer differentiation potential and plasticity in both normal and cancer stem cells[24,25]. Resistant cells exhibited significantly higher entropy compared with treatment-naïve cells (**Fig. 1E**). We further reasoned that if EMT reflects a plasticity-enabling state, it should not necessarily confer an immediate advantage but rather increase the capacity for adaptation over time. To test this, we exposed resistant (erALKi) and naïve cells to microenvironmental stresses commonly encountered within tumors: hypoxia, acidosis, and glucose starvation[26,27]. To distinguish direct drug resistance from gradually acquired adaptation, we monitored population expansion under selective pressure over time. After short-term exposure (3 days), resistant and naïve cells showed comparable survival and growth, indicating that pre-existing resistance does not account for the difference between the two populations (**Fig. 1F**). However, with prolonged exposure (≥10 days), resistant cells exhibited markedly greater expansion, revealing a time-dependent increase in adaptive capacity (**Fig. 1G** and **Fig. S1C).** A similar time-dependent pattern was observed when resistant cells were challenged with TKIs that do not directly target the oncogenic driver ALK (MEK inhibitor, trametinib[28,29]; JAK inhibitor, ruxolitinib[30]; or mTOR inhibitor, rapamycin[31]). While early responses were comparable, resistant populations progressively adapted and displayed increased growth relative to naïve cells (**Fig. 1H**). These findings demonstrate that resistance to one drug confers a generalized, plasticity-dependent capacity to adapt to unrelated pharmacological and environmental stressors.

We next asked whether this adaptive potential extends to an enhanced ability to adapt across tissue environments. Metastatic colonization represents a stringent selective bottleneck that requires plasticity-mediated adaptation[32]. To test this, we injected 1:1 mixtures of mCherry-labeled resistant cells (erLor or erAlec) and GFP-labeled naïve cells subcutaneously into the flanks of NSG mice. While both populations engrafted the primary site to comparable levels, analysis of spontaneous lung metastases by fluorescence-activated cell sorting (FACS) revealed a substantial enrichment of resistant cells, with up to twice as many mCherry+ (erLor and erAlec) as GFP+ (naïve) cells recovered from metastatic lesions (**Fig. 1I**). Control mice injected with naïve cells alone showed no such enrichment, and comparable engraftment at the flank confirmed that the effect was specific to the metastatic site. To distinguish between enhanced dissemination from the primary tumor versus superior adaptability at the metastatic site, we bypassed local invasion and intravasation by injecting resistant and naïve cells directly into the circulation via the tail vein[33]. Resistant cells again outcompeted naïve cells by two- to three-fold in lung colonization (**Fig. 1J** and **Fig. S1D**), demonstrating that resistant cells adapt more effectively to the lung microenvironment, a property consistent with enhanced plasticity.

Together, these data show that ALK inhibitor resistance converges on EMT- and stemness-associated programs, is accompanied by increased transcriptional entropy, and confers a broad adaptive capacity that extends to both pharmacological and environmental stressors *in vitro* and metastatic colonization *in vivo*. Notably, similar EMT- and stemness-related adaptations have been reported across diverse models of acquired targeted therapy resistance, including those described by Shaffer et al[34] and our collaboration with Yanai and colleagues[7], reinforcing the general relevance of this phenomenon. These findings support the hypothesis that therapeutic pressure selects for phenotypic plasticity as an enabler of resistance evolution.

Exposure to treatment or harsh environments drives gradual selection for rare cells with higher adaptability

In vitro, resistant cells displayed a growth advantage only after prolonged exposure, prompting us to ask whether gradual, multi-step resistance development might itself promote indirect selection for subpopulations with enhanced adaptability. To address this question, we developed a computational model of heterogeneous tumor cell populations under treatment, explicitly comparing two evolutionary frameworks: a single-hit model, in which resistance arises from a solitary genetic event driving rapid clonal expansion, and a multi-step model, in which resistance requires sequential modifications (**Fig. 2A**). This framework allowed us to generate predictions to guide follow-up experiments.

To capture both local and global dynamics, we implemented two complementary approaches: a spatially constrained agent-based model (ABM) (**Fig. S2A**) and a non-spatial ordinary differential equation (ODE) model (**Fig. S2B-C, Supplementary Methods**). In both frameworks, tumors were represented as populations of cells differing in their level of plasticity, which determined the probability of undergoing a resistance-driving phenotypic change. Plasticity was modeled as an abstract property capturing the combined effects of non-genetic variability, rather than as a specific molecular pathway. Individual cells could therefore transition between phenotypic states through stochastic events, allowing us to track how subpopulations evolve under treatment pressure over time.

Simulations were initialized with 10,000 cells partitioned into three phenotypic categories: 90% sensitive, lacking plasticity (mutation rate = 0), 9% with baseline plasticity (1x, defined mutator rate/fitness-change probability), and 1% with high plasticity (2x mutator rate/fitness-change probability). At each simulation step, cells could undergo one of three processes—death, division, or phenotypic change—intended to represent cumulative genetic and/or epigenetic modifications without distinguishing their molecular origin (**Fig. 2B**). Key parameters were systematically varied, including the initial frequencies of plastic subpopulations and the nature of

treatment applied. Two treatment modalities were modeled: cytostatic therapy, implemented by altering the proliferation rate (**Fig. S2B**), and cytotoxic therapy, implemented by altering the cell death rate (**Fig. S2C**).

Consistent with our initial hypothesis, we found that multi-step resistance does in fact drive the progressive selection for cells with greater adaptability. Furthermore, the simulations revealed that even modest differences in adaptive potential were sufficient to produce enrichment under treatment pressure. When the more adaptable subpopulation comprised only ~1% of the treatment-naïve population and exhibited just a twofold higher adaptability rate, it progressively expanded during therapy. In contrast, the single-hit framework yielded resistant outgrowth dominated by pre-existing resistant clones, with minimal contribution from adaptable subpopulations (**Fig. 2C** and **Fig. S2A–D**).

Together, these simulations indicate that multi-step resistance emerges through progressive selection for rare cells with intrinsically higher plasticity. This trajectory indicates that the substrate for resistance is not an isolated, single-hit event but a continuously evolving population enriched for rare, highly adaptable cells capable of incrementally improving their fitness under treatment pressure, a prediction we next tested experimentally.

Individual NSCLC clones can be classified into adaptation potentials with distinct functional and molecular profiles

To test a key assumption of our *in silico* model, that treatment-naïve populations contain subclones with variable adaptability, providing the substrate upon which selection can act, we sought experimental evidence for rare cells with enhanced capacity to tolerate and acquire resistance to unrelated stressors. We independently labeled NSCLC cells using two high-complexity DNA barcode libraries (CloneTracer[35] and CloneSweeper[36]) to trace the fate of individual lineages. Each barcoded population was then exposed to a panel of TKIs and environmental stress conditions (**Fig. 2D**) and barcode composition before and after every challenge was compared to identify lineages capable of expanding across multiple contexts.

With both libraries, our analysis revealed a rare subset of barcodes that expanded across multiple conditions, though not universally across all replicates (**Fig. 2E** and **Fig. S3A, S3C**). This variability likely reflects a combination of stochastic selection dynamics and cellular plasticity, which may enable individual lineages to discover distinct adaptive solutions, such that each resistant lineage can tolerate multiple stressors, but the specific combinations of stressors are only partially overlapping across lineages. Importantly, this notwithstanding, reproducible lineage-level patterns emerged across the independent libraries. For example, in one dataset, barcodes enriched under ceritinib, crizotinib, lorlatinib, and brigatinib clustered separately from those enriched

under alectinib and trametinib, or low pH and glucose starvation (**Fig. S3B**). While in the other library, barcodes selected by alectinib and lorlatinib grouped apart from those expanded under acidic conditions (**Fig. S3D**). These results support the view that adaptability is a consistent property of a rare subpopulation within the naïve pool capable of tolerating diverse stressors.

To directly assess adaptability at the level of individual lineages, we derived single-cell clones from treatment-naïve H3122 cells. From 127 sorted cells, 21 clonal colonies were established and challenged independently with ALKi (alectinib, lorlatinib, crizotinib, ceritinib, brigatinib). Based on growth under none, one, or multiple conditions, clones were classified as low- (LAP), intermediate- (IAP), or high-adaptation potential (HAP) (**Fig. 3A**). Crystal violet assays revealed that only 2 of 21 clones were considered as HAP cells (**Fig. 3B** and **Fig. S4A**), consistent with our barcoding data and previous reports indicating that resistant cells represent a rare subcompartment of the tumor mass[6,7,34,35]. Importantly, statistically significant differences between LAP, IAP, and HAP cells emerged only in long-term assays, whereas short-term exposure to either microenvironmental stressors (hypoxia, acidosis, glucose starvation) or TKIs (trametinib, ruxolitinib, rapamycin) revealed no distinction (**Fig. 3C**), suggesting rather than being intrinsically resistant, the HAP cells are able to adapt over time. This mirrors our earlier finding that adaptability emerges progressively rather than within a short timeframe.

Sequential clonogenic assays were performed to assess the stability of adaptation phenotypes over time. Each week, single-cell–derived lines were counted, replated, and treated continuously with ALKi for four weeks to allow resistant colony formation, followed by crystal violet staining and quantification. The phenotypes proved stable for up to 8 weeks: clones initially classified as HAP retained high adaptability, consistently forming larger and more numerous resistant colonies, whereas LAP clones maintained low adaptation potential and failed to generate resistant colonies (**Fig. S4B**). The parental population formed colonies at intermediate frequency, as expected from a heterogeneous mix of lineages. These differences were not explained by growth rate, as untreated parental, LAP, and HAP clones proliferated comparably. However, under treatment, HAP clones resumed growth after ~4 weeks, whereas LAP clones remained sensitive (**Fig. S4C**).

To molecularly characterize these phenotypes, we performed bulk RNA-seq on LAP, IAP, and HAP clones. Unsupervised clustering (**Fig. S5A**) and PCA (**Fig. S5B**) showed that clones of the same class clustered together, confirming that the categories reflect stable, molecularly distinct states. LAP clones showed the greatest heterogeneity across replicates, whereas HAP clones displayed consistent profiles. GSEA revealed that, similar to cells with evolved resistance, HAP clones upregulated EMT- and stemness-associated pathways, including TGF-β, Hedgehog, and TNFα/NF-κB (**Fig. 3D** and **Fig. S5C**)[17–23,37]. Morphologically, LAP clones retained the rounded cobblestone

appearance of parental cells, while HAP clones displayed a more mesenchymal phenotype (**Fig. S5D**).

Together, these findings demonstrate that treatment-naïve NSCLC cells are heterogeneous in adaptability, with resistance emerging from the rare fraction endowed with broad adaptive potential. At the molecular level, clones with high adaptation potential consistently display EMT- and stemness-associated signatures, suggesting that these programs may set the molecular context that enables greater adaptability. These results align with our *in silico* predictions that only a small, plastic subpopulation provides the substrate for multi-step resistance evolution under therapeutic pressure.

TKI adaptation-potential extends to metastatic potential and multi-stress resistance

After deriving and characterizing LAP, IAP, and HAP clones *in vitro*, we next validated their phenotypes *in vivo.* NSG mice were implanted subcutaneously with either LAP or HAP cells and treated with alectinib to monitor resistance dynamics. For the first six weeks, LAP- and HAP-derived tumors showed comparable sensitivity; however, over longer time frames, HAP tumors developed resistance whereas LAP tumors remained sensitive (**Fig. 3E**). To determine whether LAP tumors harbored minimal residual disease or had been fully eradicated, treatment was withdrawn. Residual disease regrew, but upon re-exposure to alectinib the LAP tumors remained sensitive, confirming that LAP cells fail to acquire resistance even after prolonged treatment.

Because naïve HAP clones shared molecular and morphological features with fully resistant erLor and erAlec cells, we next asked whether they also exhibited increased metastatic potential. LAP, HAP, and parental cells were engineered to secrete Cypridia luciferase (C-luciferase)[38], enabling sensitive longitudinal monitoring of metastatic burden after tail-vein injection (**Fig. 4A**). Besides in the lung, which is the expected metastatic site, most animals also developed liver tumors (**Fig. S6A**). By 15 weeks, mice injected with HAP cells exhibited strong luciferase signal, indicating robust metastatic colonization, whereas plasma luciferase in LAP-injected mice remained below the detection threshold (**Fig. 4B**). Parental cells also formed metastases, but with delayed kinetics compared to HAP cells (**Fig. 4B**). These findings demonstrate that high adaptability confers not only resistance, but also increased metastatic potential.

Similar to our previous testing of erLor and erAlec cells in conditions common in the solid tumor microenvironment (**Fig. 1G**), we tested the ability for LAP, IAP, and HAP cells to adapt under the same conditions (**Fig. 4C**). In the same way, we tested whether adaptation-potential classifications were maintained across non-ALK TKIs (**Fig. 4D**). As these cells require time to adapt, the difference in adaptation potential is only evident in the longer-term experiments. HAP cells can develop more resistant colonies in the long-term than the Parental or LAP populations. The LAP cells consistently have no to very

low growth under any drug condition even over longer time scales. Thus, the ability to adapt to ALKi remains consistent in orthogonal stressors.

Motif enrichment analysis informs therapeutic vulnerabilities to modulate adaptation potential

Chromatin accessibility influences the ability of cells to adapt by regulating transcriptional responses to environmental change[39]. To test whether plasticity in our samples is reflected at the chromatin level, we performed bulk ATAC-seq[40]. Unsupervised clustering of the top 500 most variable regions grouped biological replicates together, consistent with similar chromatin accessibility landscapes within each group (**Fig. 5A**). Open chromatin in HAP cells was disproportionately associated with developmental and differentiation programs, indicating preferential accessibility of regulators that control cell state transitions and thereby support phenotypic plasticity (**Fig. S6B-C**). Motif enrichment analysis further showed that HAP-specific accessible regions were enriched for regulators of EMT and stemness, including KLF4 and SOX family members, whereas LAP-specific motifs corresponded to housekeeping and maintenance programs (**Fig. 5B** and **Fig. S6B-C**).

Based on these findings, we next asked whether plasticity could be induced in LAP cells by experimentally reprogramming their cell state. Expression of Yamanaka factors (*Oct3/4, Sox2, Klf4, c-Myc*; OSKM) is known to reprogram somatic cells into pluripotent stem cells[16], leading us to hypothesize that even partial induction of these factors might increase adaptability and reduce sensitivity to ALKi. Indeed, when challenged with ALKi for 15 days, LAP+OSKM cells followed the growth trajectory of evolved resistant cells rather than parental, LAP, or HAP lines (**Fig. 5C**). Given the link between EMT and increased plasticity, we next asked whether enforcing EMT could reproduce this phenotype. To this end, we generated LAP cells overexpressing Slug (*SNAI2,* LAP+Slug), a canonical EMT-inducing transcription factor[7,41–44]. Like LAP+OSKM, LAP+Slug cells showed reduced sensitivity to ALKi (**Fig. 5C**). Both manipulations induced a morphological shift toward a more mesenchymal phenotype (**Fig. S6D**). These findings demonstrate that adaptability in LAP cells can be experimentally enhanced by partial reprogramming through either stemness or EMT programs.

Conversely, we asked whether the adaptive capacity of HAP cells could be diminished by restricting access to plasticity-associated regulators. Guided by our ATAC-seq results, we introduced shRNAs targeting SOX2 (HAP+ shSOX2). Knockdown of SOX2 alone did not restore full drug sensitivity, but significantly reduced the proportion of cells that acquired resistance in long-term assays, without affecting short-term growth (**Fig. 5D** and **Fig. S6E**). These data show that the evolvability of HAP cells can be suppressed by limiting transcription factors that sustain plasticity.

Because HAP and LAP cells show comparable short-term sensitivity to ALKi, we hypothesized that epigenetic inhibitors might prevent highly adaptable HAP cells from undergoing gradual state transitions thereby maintaining them in a drug-sensitive state. To test this, we treated HAP cells with either the histone deacetylase (HDAC) inhibitor panobinostat[45,46] or the histone acetyltransferase (HAT) inhibitor A485[47]. Doses were selected to avoid direct cytotoxicity but high enough to induce cellular stress, as confirmed by decreased NRF2 (*NFE2L2*) expression (**Fig. S6F**). Cells were then plated into ALKi under three conditions: untreated, pretreated for 7 days with epigenetic inhibitor, or continuously co-treated with both the epigenetic inhibitor and ALKi. In both pretreated and co-treated groups, panobinostat prolonged ALKi sensitivity, whereas untreated HAP cells eventually escaped therapy (**Fig. 5E** and **Fig. S6G**). A485 produced similar results (**Fig. S6H**) which may be due to both HDAC and HAT inhibitors blocking core regulatory transcription factor genes[48]. These findings indicate that pharmacologic interference with chromatin regulators can suppress the gradual development of resistance by blocking adaptive reprogramming.

Together, these experiments establish that phenotypic plasticity is encoded in the chromatin landscape, can be experimentally increased or suppressed, and can be pharmacologically restrained. By showing that resistance evolves not from pre-existing, intrinsically resistant clones but through the progressive selection of rare, highly plastic cells, our findings redefine how therapeutic pressure sculpts tumor evolution and point to plasticity itself as a central, targetable driver of resistance.

DISCUSSION

Across cancers, acquired resistance to targeted therapy has been linked to EMT and stemness programs, increased metastatic potential, and tolerance to chemotherapy and radiotherapy[49]. These recurring observations motivated our hypothesis that resistance might arise within populations enriched for phenotypic plasticity, herein defined as an expanded capacity for therapy induced state transitions and therefore adaptability. Building on our prior finding that resistance accrues through repeated adaptation, we now show that i) therapy preferentially enriches cells with higher plasticity, that ii) the stepwise accrual of resistance amplifies selection for this trait, that iii) EMT and stemness mark and facilitate the plastic state rather than act as universal proximal drivers of escape, and that iv) plasticity can be increased or constrained by targeted perturbations.

The in silico mathematical model we constructed to interrogate this hypothesis predicted that multistep selection will preferentially expand rare subclones with greater plasticity, even when they are scarce at baseline. It further predicted that the fitness differences would not manifest early during treatment, but lead to a delayed expansion of the more plastic compartment enrichment with continued exposure. Our experiments mirrored

these population level dynamics. Lineage barcoding and single cell derived clones revealed a rare, pre-treatment fraction with higher adaptation potential that expanded under sustained pressure. Short term responses were similar across lineages, but over longer intervals the higher plasticity fraction recovered, adapted to pharmacologic and microenvironmental stressors, and colonized the lung more efficiently *in vivo*.

Crucially, these results refine how EMT and stemness should be interpreted in the context of resistance. Rather than serving as universal, proximal mechanisms of escape, EMT and stemness associated programs are manifestations of a broader plasticity program that widens the repertoire of accessible cell states under selection. These frameworks may be integrated if rapid adaptation occurs over short timescales giving the appearance of direct resistance. Consistent with the plasticity-based view, the subpopulation with higher adaptation potential shows increased transcriptional entropy and preferential chromatin accessibility at developmental and cell identity regulators, features consistent with a regulatory architecture that can be reconfigured under treatment. Perturbing these identity programs alters long term outcomes without changing immediate drug sensitivity. Partial reprogramming or EMT induction increases adaptation potential in low plasticity clones, whereas limiting access to plasticity sustaining transcription factors decreases the outgrowth of resistant colonies over longer intervals. In this framework, the capacity to adopt alternative phenotypic states may represent a convergent, targetable early step on the path to resistance, and our data suggests that genetic or pharmacologic perturbation of this capacity can influence the tempo of adaptation.

Although our experiments center on non-genetic adaptation, the same principle likely extends to resistance even if attributed to genetic drivers. Plasticity enlarges the phenotypic space on which selection operates, facilitating epigenetic reconfiguration and creating opportunities for genetic alterations that stabilize fitter states. This perspective reconciles drug specific molecular heterogeneity with recurrent convergence on shared functional properties. Distinct ALK inhibitors drive divergent transcriptional states, yet resistant populations display cross ALK inhibitor tolerance together with EMT and stemness features, consistent with selection operating on plasticity rather than on a single pathway.

The tumor microenvironment is likely to shape these dynamics. Hypoxia, acidosis, nutrient limitation, and paracrine signaling through pathways such as TGF-β and NF-κB can remodel chromatin and redirect transcriptional programs, thereby modulating plasticity and the probability of adaptation[50–52]. Consistent with niche effects, we observe inter compartment heterogeneity. Selection patterns differ between the primary site and metastatic sites, and resistant or higher plasticity cells show superior colonization of the lung relative to naïve counterparts. These observations support a link between therapy induced adaptation and metastatic competence.

This work focuses on ALK-rearranged NSCLC in long-term culture and xenograft models. Future studies should test how broadly these principles extend to other genetic backgrounds, tissues and immune-competent settings, with more detailed molecular and quantitative dissection of plasticity.

These findings are of translational value. If treatment selects for plasticity, timing and composition become levers. Agents that stabilize cell identity or restrict reprogramming prolonged sensitivity to targeted inhibitors in our models, supporting that schedules that target the adaptation window when reconfiguration, rather than initial cytotoxicity, are rate limiting. Composite biomarkers of plasticity, including entropy based metrics, EMT and stemness gene sets, motif level chromatin signatures, and functional stress adaptation assays, could stratify risk and guide trials designed to restrain adaptive reprogramming and to capture delayed adaptation as an endpoint[53,54]. Although our emphasis is on epigenetic routes, the framework is compatible with genetics driven resistance by positing plasticity as a rate limiting resource for both non genetic tolerance and subsequent genetic change.

In sum, repeated adaptation under therapeutic pressure increases the representation of cells with greater phenotypic plasticity. EMT and stemness associated programs often facilitate this capacity but are not, in most contexts, sufficient on their own to confer durable escape. Recognizing plasticity as the trait under selection provides a coherent account of delayed resistance, recurrent transcriptional convergence, and site-specific behavior, and supports evolution informed strategies that stabilize identity, modulate paracrine drivers, and constrain adaptive trajectories.

METHODS

Cell culture

NSCLC cell line H3122 was obtained from the Lung Cancer Center of Excellence Cell Line depository at Moffitt Cancer Center. H3122 cells were grown in RPMI-1640 containing L-Glutamine (Gibco), supplemented with 10% fetal bovine serum (FBS), 1% penicillin- streptomycin, and 10µg/ml human recombinant insulin (Gibco). Cells were incubated at 37℃ with 5% CO_2 atmosphere with constant humidity. Cells were passaged as needed using 0.25% trypsin (Gibco). Passage number was kept below 15 passages to maintain consistency in phenotypes.

Derivation of erLor and erAlec cells

As detailed in Vander Velde (2020)[6], H3122 cells were subjected to continuous high ALKi concentrations of 2.0uM alectinib or 2.0uM lorlatinib (Fisher Scientific).

Single-cell Clones derivation

H3122 cells were detached using accutase (Gibco), passed through cell strainers and subjected to sterile flow sorting (BD FACSAria II) to obtain single-cell droplets into six 96-well plates. After careful microscopic evaluation at 1, 3, and 5 days post sorting, we scored 24 wells that had growth from a single cell. Cells were further expanded to proceed with experiments.

Classification of single-cell derived clones into high, intermediate, or low adaptation potential

We assessed 21 single-cell derived clones' ability to evolve resistance to alectinib by long-time drug exposure at 500nM (up to 3 months). Among the 21 subclones, 2 showed high adaptation potential, 8 showed intermediate, 11 showed no adaptability scored by their confluency when we stopped the experiment. In order to confirm this preliminary observation and further assess their evolvability of resistance to other TKI's, duplicate cultures of 10,000 cells/well from each clone seeded into 24-well plates. After 24h, media was replaced with media containing 0.1% DMSO or one ALKi (0.1µM ceritinib (Fisher Scientific), 0.5 µM crizotinib (FisherScientific), 0.5 µM lorlatinib, 0.5 µM alectinib, or 0.1 µM brigatinib (AstaTech). After 40 days of culture, plates were subjected to crystal violet staining and their growth measured by ImageJ by scoring the colony area of wells covered by cells.

Functional assays

Cells were collected, counted, and plated such that the same number of cells was added to each well of the experimental plate. 24 hours after seeding, media containing the treatment, stressor, or vehicle was added and subsequently replaced every 3-4 days. Acidosis media was made by adding HCl (6N, VWR) to RPMI-1640 until the pH reached 5.5. Then the acidic media was filtered (0.2um) and the rest of the media components were added. For pseudo-hypoxia media, cobalt chloride hexahydrate ($CoCl_2$) was dissolved in PBS then added to RPMI complete media so the final concentration is 200uM. For starvation media, when stressing the evolved resistant lines, the complete media was diluted 1:10 in PBS; when stressing the single-cell derived clones, the complete media was diluted 1:5 in PBS. Cell viability was assessed using crystal violet staining followed by ImageJ quantification or elution, or through Cell Titer Glo assay following manufacturer instructions. Short term assays lasted 3-7 days, long term assays lasted 10-30 days.

Crystal violet staining

At endpoint, the plate was placed on ice and washed with ice cold PBS (Gibco). Then the cells were fixed with 100% methanol (Fisher Chemical) for 10 minutes on ice. The methanol was aspirated off and the plate was placed at room temperature before 0.5% crystal violet solution in 25% methanol was added for 10 minutes. The crystal violet

solution was removed and the plate was submerged in distilled water multiple times to remove excess stain. The plate was placed upside down to dry at room temperature. Once dry, the crystal violet stained plates were imaged on the Amsheran Imager 600 using the colorimetric trans-illumination setting.

Acetic Acid Elution

After imaging on the Amsherham Imager 600, 10% acetic acid (Fisher Chemical BP2401-500, diluted in double-distilled water) was added to each well, 50ul for a 96-well plate, or 200ul for a 48-well plate. The plate was placed on a shaker for 15 minutes to agitate and elute the crystal violet staining. Then, the acetic acid and crystal violet mixture was diluted with distilled water in a 1:4 ratio. In a new 96-well white-walled clear-bottom plate, 100ul of the solution in each well of the original plate was transferred to a new well in the new plate. The BioTek Synergy Microplate reader read the plate at 590nm. All values were normalized to mean absorbance in DMSO.

ImageJ quantification

To analyze the image from the Amsherham Imager 600 using ImageJ, the oval selection tool was used to select a single well. The image was then converted to 16-bit. Next, the "Analyze" menu was used to select "Measure" to measure the entire area of the selected well. Then, the "Image" menu was used to select "Adjust" followed by "Threshold." The red mask is used to select empty spaces before selecting “Analyze" and "Measure" again to measure the red area. Subtract the red area from the entire area which was measured first to get the desired measurement.

Cell Titer Glo Assay

Cell viability was assessed using CellTiterGlo reagent (Promega) following the manufacturers protocol and detected using the luminescence setting on a GloMax luminometer (Promega).

Cell imaging

Brightfield images were taken on a Zeiss AXIO Observer Z1 microscope to examine cell morphology. For imaging of ex vivo resistant and parental cells, fluorescent channels of 610nm (mCherry) and 509nm (GFP) were used to differentiate between cell lines.

CloneTracer

H3122 cells were transduced at 30% efficiency (as defined by fluorescence-activated cell sorting analysis of dsRed expression) with CloneTracer neutral DNA barcode library, kindly provided by Frank Stegmeier (Addgene #67267). Barcode-containing cells were selected with puromycin and expanded for 7 days. Barcoded cells were collected and split into conditions. Triplicate cultures of 100,000 cells each were plated into 6-well

plates in the presence of 0.1% DMSO, 0.5 μM crizotinib, 0.5 μM alectinib, and 0.5 μM lorlatinib, 0.1 μM ceritinib, 0.1 μM brigatinib, 0.1 μM trametinib, starvation, or acidosis conditions. One aliquot of 100,000 cells was frozen to serve as an initial time point. Cells were collected following 4-8 weeks of cell culture based on their growth in different conditions. Genomic DNA was extracted using proteinase K digest, followed by phenol–chloroform purification. Barcodes were amplified, sequenced, and analyzed following protocols described in ([35]) and an updated procedure provided on the Addgene website https://www.addgene.org/ pooled-library/clontracer. PCR amplification was done with the protocol provided by Stegmier lab, 30 cycles using second-generation ClonTracer primers with the following sequence: 5′-CAA GCA GAA GAC GGC ATA CGA GAT-Variable Sequence-GTG ACT GGA GTT CAG ACG TGT GCT CTT CCG ATC TCT AGC ACT AGC ATA GAG TGC GTA GCT-3′.

CloneSweeper

H3122 cells were transduced at 5% efficiency, as defined by fluorescence-activated cell sorting analysis of GFP expression, with the neutral DNA barcode library, kindly provided by Shaffer Lab ([36]). Cells containing barcodes were cultured for 12 days and then divided into treatment groups of 200,000 cells per 10 cm plate. Treatments included DMSO (0.05%), lorlatinib (0.5 μM), alectinib (0.5 μM), or medium adjusted to pH 5.5. An additional aliquot of 200,000 cells was frozen to serve as an initial timepoint. Four plates were prepared for each treatment condition. One plate was harvested and frozen two weeks after treatment initiation to look at intermediate resistance abundance, while the remaining plates were collected once confluent, approximately four weeks for the pH 5.5 condition and five weeks for the lorlatinib and alectinib treatments. Barcode sequences were amplified, sequenced, and analyzed according to the genomic DNA barcode sequencing protocol described in ([36]).

Barcode enrichment analysis

For each library, distinct barcode sequences and their corresponding read counts were summarized and merged into a unified count matrix in R (v4.4.0). To account for differences in sequencing depth, barcode counts were normalized to the total number of reads per sample, yielding relative barcode abundances. The resulting normalized and raw count matrices were used for enrichment and comparative evaluations. Barcodes with a frequency above 0.001 in at least 2 samples were kept for further analysis.

Lentiviral overexpression of Yamanaka factors and Slug

Lentiviral vector for inducible overexpression of *Oct4, Klf4, Myc and Sox2* (OSKM; FUW-tetO-hOKMS) was a gift from Tarjei Mikkelsen (Addgene #51543). Lentiviral vector for inducible expression of *Slug* (Addgene #82162) was Gateway-cloned under a doxycycline induced promoter on a pInducer20 backbone (Addgene #44012). JetPrime

reagents and protocol (Polyplus) were followed for transfection into HEK-293T packaging cells. Virus-containing supernatant was collected 24-48h after transfection and filtered through 0.45µm filters (Corning). H3122 low adaptation-potential derivatives were infected with viral lysate containing polybrene (Santa Cruz Biotechnology) before selection in the appropriate antibiotic. To induce expression of either Yamanaka factors or Slug, doxycycline was added to the cell medium for 30 days prior to experiment initiation.

shRNA knockdown for SOX2

SOX2 inducible lentiviral small hairpin RNA (shRNA) (Tet-pLKO-puro-SOX2) was a gift from Charles Rudin (Addgene #47540). JetPrime reagents and protocol (Polyplus) were followed for transfection into HEK-293T packaging cells. Virus-containing supernatant was collected 24-48h after transfection and filtered through 0.45µm filters (Corning). H3122 high adaptation-potential derivates were infected with viral lysate containing polybrene (Santa Cruz Biotechnology) before selection in the appropriate antibiotic. To induce *SOX2* knockdown, doxycycline was added to the cell medium for 7 days prior to experiment initiation.

Treatment with Epigenetic Inhibitors

HAP cells were pre-treated with either vehicle (DMSO) or an epigenetic inhibitor A485 (4µM, MedChem Express) or Panobinostat (2 µM, Fisher) for 7 days prior to exposure to ALKi. One arm was co-treated with the epigenetic inhibitor and ALKi to make a total of 3 groups: 1) HAP pretreated with DMSO, then treated with ALKi, ii) HAP pre-treated with epigenetic inhibitor, then treated with ALKi, iii) HAP pre-treated with DMSO, then co-treated with ALKi and epigenetic inhibitor.

PCR

RNA extraction was performed with RNAeasy (Qiagen) according to the manufacturer's instructions. Quantitative reverse transcriptase real-time PCR was performed using SensiFAST SYBR Hi-ROX One-Step Kit (Meridian Biosciences, BIO-73005) on a QuantStudio 7 Pro (ThermoFisher). Primer sequences: *NFE2L2* FW, 5'-GAGAGCCCAGTCTTCATTGC-3'; *NFE2L2* RV, 5'-TTGGCTTCTGGACTTGGAAC -3'; *RPL19* FW, 5'-GATCCGGAAGCTCATCAAAG -3', *RPL19* RV, 5'-GGCTGTACCCTTCCGCTTAC -3'.

Live Cell Imaging

Cells were plated and allowed to attach for 24 hrs before treatment with either vehicle (DMSO, 0.05%), lorlatinib (0.5µM), or alectinib (0.5µM) along with an epigenetic inhibitor if indicated. Culture medium and drugs were changed every 3 days. Sartorius

Incucyte 2020 was used to take images of each well at least every 3 days, and to analyze the images.

In vivo metastasis subcutaneous

erALKi expressing mCherry and Parental cells expressing GFP or mCherry a 1:1 mixture of erLor:Parental, erAlec:Parental, or Parental (GFP): Parental (mCherry) in RPMI media. Type 3 matrigel was added to each sample in equal volume to the media. The mice were anesthetized with 4% isoflurane for induction, and anesthesia maintenance with 2% isoflurane. 100ul of the cells with matrigel were injected per flank, with 1 million cells per flank. After 4 weeks, both the subcutaneous tumor site and lungs were harvested for flow cytometry analysis. Xenograft studies were performed in accordance with the guidelines of the Institutional Animal Care and All the xenograft studies were performed per the approved procedures of IACUC protocol IS00013344 of the H. Lee Moffitt Cancer Center. Animals were maintained under AAALAC-accredited specific pathogen-free housing vivarium and veterinary supervision following standard guidelines for temperature and humidity, with a 12-hour light/12-hour dark cycle.

In vivo metastasis tail vein

erALKi expressing mCherry and Parental cells expressing nuclear GFP or mCherry were prepared. Once counted, a 1:1 mixture of erLor:Parental, erAlec:Parental, or Parental (GFP): Parental (mCherry) in RPMI media. 100ul of the cell-containing media with 100,000 cells per mouse were injected via tail vein. After 4 weeks, the lungs were harvested for flow cytometry analysis.

In vivo subcutaneous tumors

Aliquots of LAP and HAP cells were prepared with equal volume RPMI media and type 3 matrigel. 375,000 cells were injected per flank. Tumors were allowed to grow until palpable, and alectinib 25mg/kg was delivered daily via gavage. Tumor measurements were taken weekly using electronic calipers. Detection threshold is based on inadequate caliper purchase around lesion. After 19 weeks on alectinib, all three mice bearing HAP-tumors, and one mouse bearing LAP tumors were euthanized and tumors were collected. The remaining 3 mice bearing LAP-tumors were placed on a treatment holiday for 10 weeks until tumors enlarged and were then restarted on alectinib 25mg/kg.

Tumor digestion and homogenization

Tumors or lungs were digested in RPMI media supplemented with 1 mg/ml collagenase IV (Worthington),1 mg/ml hyaluronidase (Sigma), and 2 mg/ml bovine serum albumin (Fisher Scientific) at 37 °C. After neutralizing with PBS, the tumor solution was filtered with a cell strainer and centrifuged at 1000rpm for 5 minutes. Supernatant was

discarded, and cells were either immediately plated for *in vitro* culture, or resuspended in freezing media (40%RPMI complete, 50%FBS, 10%DMSO) and placed in cryovials at - 80 °C.

Flow cytometry analysis

Tumors or lungs containing GFP/mCherry mixes were digested in RPMI supplemented with 1 mg/ml collagenase IV (Worthington),1 mg/ml hyaluronidase (Sigma), and 2 mg/ml bovine serum albumin (Fisher Scientific) at 37 °C. Pellets were suspended in PBS and 0.1 µg/ml DAPI (Sigma). Percent of population that is mCherry+ and GFP+ was determined using a MACSQuant Flow Cytometer.

Plasma luciferase

Gateway cloning (Invitrogen) was used to generate plasmids with pLenti 6.3 backbone (Invitrogen) and C-luciferase (ThermoFisher, cat:16150). JetPrime reagents and protocol (Polyplus) were followed for transfection into HEK-293T packaging cells. Virus-containing supernatant was collected 24-48h after transfection and filtered through 0.45µm filters (Corning). H3122 cells were infected with viral lysate containing polybrene (Santa Cruz Biotechnology) before selection in the appropriate antibiotic. After selection, luciferase expression was checked by collecting 200ul of the conditioned media after 6 hours. The C-luciferase assay was then conducted.

***In vivo* luciferase monitoring**

LAP, HAP, or Parental cells secreting C-luciferase were prepared for injection such that 100,000 cells were injected via tail vein per mouse. Every two weeks, blood from the tail vein of each mouse was collected into ethylenediaminetetraacetic acid (EDTA) -coated tubes (ThermoScientific) and centrifuged at 2000g for 10 minutes. The plasma was collected and diluted at 1:100 with PBS before the C-luciferase assay was conducted.

C-Luciferase Assay

Vargulin, cyprindina luciferase (NanoLight Technologies), was prepared in 0.5mg/ml stock in acidified methanol (5ul of 6N HCL per 1ml methanol). A 1:1000 dilution of stock luciferase was prepared in PBS to make working concentrations. In triplicate, 20ul of the conditioned media or diluted plasma sample was plated in a white-walled 96-well plate. The assay was run with 100ul of luciferase added per well with an integration time of 2 seconds.

Bulk RNA-seq

Duplicate cultures of H3122 parental cells and single-cell derived clones were cultured until 60-70% confluent, then lysed directly by adding RNA lysis buffer. RNA was isolated for parental cells and single-cell clones using an RNAEasy Minikit (Qiagen). Reads

were generated using a Novaseq illumina platform at 30,000,000 reads per sample. Alignment was achieved using HiSat2 and the human hg19 reference genome. Normalized reads were obtained from DeSeq2. Additional unsupervised clustering and PCA analysis was performed using R.

Gene set enrichment analysis

GSEA was used to determine the gene sets enriched in high, intermediate and low evolvable clones versus parental cell line RNA-seq profiles. We used the MSigDB Hallmark [PMID: 26771021] as the predefined gene sets and performed 10,000 permutations by gene set to determine the p-values. Gene sets with false discovery rate q-value ≤0.25 were considered as significantly enriched.

Single cell transcriptome analysis

Data was originally reported in Vander Velde (2020)[6], briefly, cells were exposed to either no treatment (naive), or to 112 days of lorlatinib or alectinib. Approximately 1,000 cells were collected per sample and processed using the 10X Genomics pipeline on the Illumina NextSeq 500 instrument. In this article, the data has been further analyzed by Gini Score.

Gini Analysis

Single cell transcriptomic data was analyzed using the “DescTools” and “Seurat” packages on R.

ATAC-seq

Duplicate cultures of H3122 parental cells and cell-line derivatives (two clones from each category such as high, intermediate and low adaptability potential clones, and two independently derived erLor and erAlec replicates) were cultured in complete RPMI until 60-70% confluent. Cells were collected and frozen. ATAC-sequencing was performed by ActiveMotif for at least 50,000 reads. Usable reads were aligned to the hg38 reference genome. Bioinformatic analysis was done in collaboration with Berkley Gryder using a previously established pipeline which can be found at https://github.com/GryderLab/gryderlab_pipeline. Briefly, ATAC-seq reads were matched with bulk RNA-seq data from the same clone. Motif enrichment analysis was performed using HOMER and biological processes were identified using ToppGene. Biological processes with p-value less than $1x10^{-6}$ were considered significant.

Computational Model

The agent-based model (ABM) includes three cell types—sensitive, baseline-plasticity persisters, and high-plasticity persisters—each capable of proliferation and death. Division and death rates depend on treatment status and local environmental conditions

(Supplementary Methods). Mutations arise stochastically at division and are assumed beneficial, providing incremental fitness gains toward resistance. Mutations are mechanism-agnostic (genetic or epigenetic) and occur only upon division. Treatment is modeled as a binary, domain-wide perturbation: sensitive cells are fully inhibited and rapidly decline, while persister populations maintain net-zero growth until resistance mutations appear.

The ABM is implemented on a 10,000-site two-dimensional grid. Agents interact with their local environment through a Moore neighborhood of eight adjacent sites. Initial populations are randomly seeded according to experimentally or theoretically motivated proportions. At each discrete time step, agents update asynchronously following probabilistic rules for division, death, and mutation. Fifty independent stochastic realizations were run to capture variability.

To complement the ABM and isolate the effects of stochasticity and spatial structure, a deterministic ODE model was developed under identical biological assumptions and rate parameters, modeling population-level dynamics with a carrying capacity of 1,000 cells.

Python was used for parameter estimation, data processing, visualization, and to implement both the ABM and ODE models. The ODE simulations, being deterministic, were run once per parameter set. All simulation scripts, parameter files, and analysis notebooks are publicly available at https://github.com/mfroid/plasticityModels/. All ABM data is available upon request from the authors. See **Supplemental Methods** for additional information.

Statistical Analyses

Statistical analysis was performed with Prism 10 (GraphPad) or R statistical software. Details of statistical tests are provided in Supplementary Table 1. *p<0.05, **p<0.01, ***p<0.001, and ****p<0.0001.

DATA AND CODE AVAILABILITY

- All simulation scripts, parameter files, and analysis notebooks are publicly available at https://github.com/mfroid/plasticityModels/. All ABM data is available upon request from the authors.
- ATAC-seq data is publicly available at https://www.ncbi.nlm.nih.gov/sra/PRJNA1400308. The previously established analysis pipeline can be found at https://github.com/GryderLab/gryderlab_pipeline.
- CloneTracer and CloneSweeper datasets can be found at https://www.ncbi.nlm.nih.gov/sra/PRJNA1400309.
- Single Cell RNA sequencing data was previously reported in (6) and can be found at https://www.ncbi.nlm.nih.gov/geo/query/acc.cgi?acc=GSE144282.

- Bulk RNA sequencing data can be found at https://www.ncbi.nlm.nih.gov/sra/PRJNA1400309.
- All data reported in this paper are available from the corresponding author upon request.

AUTHOR CONTRIBUTIONS

AM conceived of the project. AB and XA designed and performed wet-lab experiments and data analysis. MF, RBC, and JM, designed and performed *in silico* experiments under the supervision of AM, JC, and DB. JR performed growth rate assays under the supervision of AB and AM. XA generated the bulk RNA-seq samples and performed the analysis. XA performed the Clone Tracer experiment and analyzed it with VT. RV contributed to making the CloneSweeper technology and liaised our use of it. AB performed the CloneSweeper experiment. AB generated the ATAC-seq samples and performed the analysis under the supervision of BG. AB, VT, and AM designed the schematics. AB, VT, and AM wrote the manuscript. JC, DB, AA, and VT made substantial input to the direction, design, and execution of the project. All authors reviewed the manuscript.

ACKNOWLEDGEMENTS

We thank M. Henry for their contribution to the animal work. This work has been supported in part by the Flow Cytometry Core and the Molecular Genomics Core at the H. Lee Moffitt Cancer Center and Research Institute.

DECLARATIONS OF INTEREST

The authors declare no competing interests.

REFERENCES

1. Strebhardt, K. & Ullrich, A. Paul Ehrlich's magic bullet concept: 100 years of progress. *Nat. Rev. Cancer* **8**, 473–480 (2008).
2. Reck, M. & Rabe, K. F. Precision Diagnosis and Treatment for Advanced Non–Small-Cell Lung Cancer. *N. Engl. J. Med.* **377**, 849–861 (2017).
3. Huang, L., Jiang, S. & Shi, Y. Tyrosine kinase inhibitors for solid tumors in the past 20 years (2001–2020). *J. Hematol. Oncol.J Hematol Oncol* **13**, 143 (2020).
4. Lung Cancer Survival Rates | 5-Year Survival Rates for Lung Cancer. *American Cancer Society* https://www.cancer.org/cancer/types/lung-cancer/detection-diagnosis-staging/survival-rates.html.
5. Ramos, P. & Bentires-Alj, M. Mechanism-based cancer therapy: resistance to therapy, therapy for resistance. *Oncogene* **34**, 3617–3626 (2015).
6. Vander Velde, R. *et al.* Resistance to targeted therapies as a multifactorial, gradual adaptation to inhibitor specific selective pressures. *Nat. Commun.* **11**, 2393 (2020).
7. França, G. S. *et al.* Cellular adaptation to cancer therapy along a resistance continuum. *Nature* **631**, 876–883 (2024).

8. Scarborough, J. A. *et al.* Identifying States of Collateral Sensitivity during the Evolution of Therapeutic Resistance in Ewing's Sarcoma. *iScience* **23**, (2020).
9. Mani, S. A. *et al.* The Epithelial-Mesenchymal Transition Generates Cells with Properties of Stem Cells. *Cell* **133**, 704–715 (2008).
10. Lambert, A. W. & Weinberg, R. A. Linking EMT programmes to normal and neoplastic epithelial stem cells. *Nat. Rev. Cancer* **21**, 325–338 (2021).
11. Grinat, J. *et al.* The epigenetic regulator Mll1 is required for Wnt-driven intestinal tumorigenesis and cancer stemness. *Nat. Commun.* **11**, 6422 (2020).
12. Fukuda, K. *et al.* Epithelial-to-Mesenchymal Transition Is a Mechanism of ALK Inhibitor Resistance in Lung Cancer Independent of ALK Mutation Status. *Cancer Res.* **79**, 1658–1670 (2019).
13. Deng, S. *et al.* Ectopic JAK–STAT activation enables the transition to a stem-like and multilineage state conferring AR-targeted therapy resistance. *Nat. Cancer* **3**, 1071–1087 (2022).
14. Holohan, C., Van Schaeybroeck, S., Longley, D. B. & Johnston, P. G. Cancer drug resistance: an evolving paradigm. *Nat. Rev. Cancer* **13**, 714–726 (2013).
15. Singh, A. & Settleman, J. EMT, cancer stem cells and drug resistance: an emerging axis of evil in the war on cancer. *Oncogene* **29**, 4741–4751 (2010).
16. Takahashi, K. *et al.* Induction of Pluripotent Stem Cells from Adult Human Fibroblasts by Defined Factors. *Cell* **131**, 861–872 (2007).
17. Jiang, C. *et al.* Innate immunity and the NF-κB pathway control prostate stem cell plasticity, reprogramming and tumor initiation. *Nat. Cancer* 1–22 (2025) doi:10.1038/s43018-025-00994-3.
18. Cammareri, P. *et al.* Loss of colonic fidelity enables multilineage plasticity and metastasis. *Nature* 1–10 (2025) doi:10.1038/s41586-025-09125-5.
19. Lee, J. H. *et al.* TGF-β and RAS jointly unmask primed enhancers to drive metastasis. *Cell* **187**, 6182-6199.e29 (2024).
20. Xu, J., Lamouille, S. & Derynck, R. TGF-β-induced epithelial to mesenchymal transition. *Cell Res.* **19**, 156–172 (2009).
21. Yeh, H.-W. *et al.* PSPC1 mediates TGF-β1 autocrine signalling and Smad2/3 target switching to promote EMT, stemness and metastasis. *Nat. Cell Biol.* **20**, 479–491 (2018).
22. Kim, B. N. *et al.* TGF-β induced EMT and stemness characteristics are associated with epigenetic regulation in lung cancer. *Sci. Rep.* **10**, 10597 (2020).
23. Su, J. *et al.* TGF-β orchestrates fibrogenic and developmental EMTs via the RAS effector RREB1. *Nature* **577**, 566–571 (2020).
24. O'Hagan, S., Wright Muelas, M., Day, P. J., Lundberg, E. & Kell, D. B. GeneGini: Assessment via the Gini Coefficient of Reference "Housekeeping" Genes and Diverse Human Transporter Expression Profiles. *Cell Syst.* **6**, 230-244.e1 (2018).
25. Torre, E. *et al.* Rare Cell Detection by Single-Cell RNA Sequencing as Guided by Single-Molecule RNA FISH. *Cell Syst.* **6**, 171-179.e5 (2018).
26. Estrella, V. *et al.* Acidity Generated by the Tumor Microenvironment Drives Local Invasion. *Cancer Res.* **73**, 1524–1535 (2013).
27. Pavlova, N. N., Zhu, J. & Thompson, C. B. The hallmarks of cancer metabolism: Still emerging. *Cell Metab.* **34**, 355–377 (2022).

28. Gilmartin, A. G. *et al.* GSK1120212 (JTP-74057) Is an Inhibitor of MEK Activity and Activation with Favorable Pharmacokinetic Properties for Sustained In Vivo Pathway Inhibition. *Clin. Cancer Res.* **17**, 989–1000 (2011).
29. Blumenschein, G. R. *et al.* A randomized phase II study of the MEK1/MEK2 inhibitor trametinib (GSK1120212) compared with docetaxel in KRAS-mutant advanced non-small-cell lung cancer (NSCLC). *Ann. Oncol.* **26**, 894–901 (2015).
30. Verstovsek, S. *et al.* Safety and Efficacy of INCB018424, a JAK1 and JAK2 Inhibitor, in Myelofibrosis. *N. Engl. J. Med.* **363**, 1117–1127 (2010).
31. Li, J., Kim, S. G. & Blenis, J. Rapamycin: One Drug, Many Effects. *Cell Metab.* **19**, 373–379 (2014).
32. Lambert, A. W., Zhang, Y. & Weinberg, R. A. Cell-intrinsic and microenvironmental determinants of metastatic colonization. *Nat. Cell Biol.* **26**, 687–697 (2024).
33. Combined Use of Tail Vein Metastasis Assays and Real-Time In Vivo Imaging to Quantify Breast Cancer Metastatic Colonization and Burden in the Lungs. https://app.jove.com/v/60687/combined-use-tail-vein-metastasis-assays-real-time-vivo-imaging-to.
34. Shaffer, S. M. *et al.* Rare cell variability and drug-induced reprogramming as a mode of cancer drug resistance. *Nature* **546**, 431–435 (2017).
35. Bhang, H. C. *et al.* Studying clonal dynamics in response to cancer therapy using high-complexity barcoding. *Nat. Med.* **21**, 440–448 (2015).
36. Shaffer Lab. CloneSweeper. *Manuscript in Preparation* (2026).
37. Yue, D. *et al.* Hedgehog/Gli promotes epithelial-mesenchymal transition in lung squamous cell carcinomas. *J. Exp. Clin. Cancer Res.* **33**, 34 (2014).
38. Charles, J. P. *et al.* Monitoring the dynamics of clonal tumour evolution in vivo using secreted luciferases. *Nat. Commun.* **5**, 3981 (2014).
39. Li, D. *et al.* Chromatin Accessibility Dynamics during iPSC Reprogramming. *Cell Stem Cell* **21**, 819-833.e6 (2017).
40. Buenrostro, J. D., Giresi, P. G., Zaba, L. C., Chang, H. Y. & Greenleaf, W. J. Transposition of native chromatin for fast and sensitive epigenomic profiling of open chromatin, DNA-binding proteins and nucleosome position. *Nat. Methods* **10**, 1213–1218 (2013).
41. Chang, T.-H. *et al.* Slug Confers Resistance to the Epidermal Growth Factor Receptor Tyrosine Kinase Inhibitor. *Am. J. Respir. Crit. Care Med.* **183**, 1071–1079 (2011).
42. Guo, W. *et al.* Slug and Sox9 Cooperatively Determine the Mammary Stem Cell State. *Cell* **148**, 1015–1028 (2012).
43. Sun, Y., Song, G.-D., Sun, N., Chen, J.-Q. & Yang, S.-S. Slug overexpression induces stemness and promotes hepatocellular carcinoma cell invasion and metastasis. *Oncol. Lett.* **7**, 1936–1940 (2014).
44. Moon, J. H., Lee, S. H. & Lim, Y. C. Wnt/β-catenin/Slug pathway contributes to tumor invasion and lymph node metastasis in head and neck squamous cell carcinoma. *Clin. Exp. Metastasis* **38**, 163–174 (2021).
45. Qian, D. Z. *et al.* Targeting Tumor Angiogenesis with Histone Deacetylase Inhibitors: the Hydroxamic Acid Derivative LBH589. *Clin. Cancer Res.* **12**, 634–642 (2006).
46. Ellis, L. *et al.* Histone deacetylase inhibitor panobinostat induces clinical responses with associated alterations in gene expression profiles in cutaneous T-cell

lymphoma. *Clin. Cancer Res. Off. J. Am. Assoc. Cancer Res.* **14**, 4500–4510 (2008).
47. Shendy, N. A. M. *et al.* Group 3 medulloblastoma transcriptional networks collapse under domain specific EP300/CBP inhibition. *Nat. Commun.* **15**, 3483 (2024).
48. Gryder, B. E. *et al.* Histone hyperacetylation disrupts core gene regulatory architecture in rhabdomyosarcoma. *Nat. Genet.* **51**, 1714–1722 (2019).
49. Gupta, P. B., Pastushenko, I., Skibinski, A., Blanpain, C. & Kuperwasser, C. Phenotypic Plasticity: Driver of Cancer Initiation, Progression, and Therapy Resistance. *Cell Stem Cell* **24**, 65–78 (2019).
50. Palma, F. R. *et al.* Histone H3.1 is a chromatin-embedded redox sensor triggered by tumor cells developing adaptive phenotypic plasticity and multidrug resistance. *Cell Rep.* **43**, 113897 (2024).
51. Chakraborty, A. A. *et al.* Histone demethylase KDM6A directly senses oxygen to control chromatin and cell fate. *Science* **363**, 1217–1222 (2019).
52. Rolver, M. G. *et al.* Tumor microenvironment acidosis favors pancreatic cancer stem cell properties and in vivo metastasis. *iScience* **28**, (2025).
53. Zhang, J., Cunningham, J. J., Brown, J. S. & Gatenby, R. A. Integrating evolutionary dynamics into treatment of metastatic castrate-resistant prostate cancer. *Nat. Commun.* **8**, 1816 (2017).
54. Smalley, I. *et al.* Leveraging transcriptional dynamics to improve BRAF inhibitor responses in melanoma. *EBioMedicine* **48**, 178–190 (2019).

MAIN FIGURES

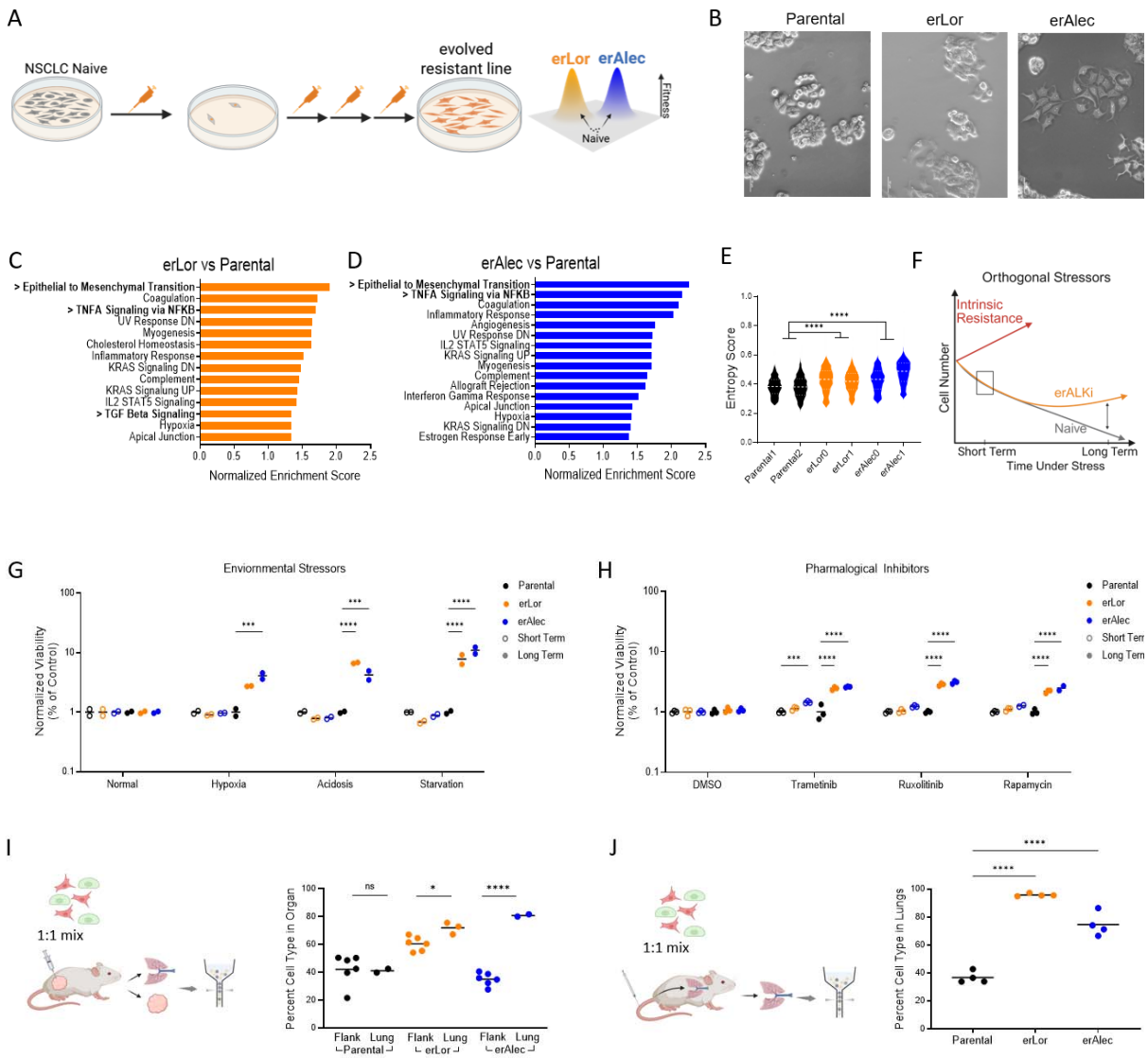

Figure 1. Independent treatment of NSCLC with different TKIs demonstrates convergence towards similar resistance phenotypes. A. Schematic of the experimental design to derive evolved resistant cells to lorlatinib (erLor) and alectinib (erAlec). **B.** Representative bright-field images of Parental, erLor, and erAlec cells in normal media at 20x magnification (Scale bar 50µm). **C.** RNA-sequencing analysis of significantly enriched pathways from Gene Set Enrichment Analysis (GSEA) of hallmark gene sets in erLor versus Parental cells or (**D**) erAlec vs Parental cells. Pathways with ≥1.33 normalized enrichment score (NES) shown. **E.** Violin plot of Gini score of transcriptional entropy for RNA sequencing data of two biological replicates each of Parental, erLor, and erAlec. One-way ANOVA with Tukey's multiple comparisons test. **F.** Schematic of expected results of short and long term experiments contrasting intrinsic and acquired resistance. **G.** Quantification of viability staining after short term or long term treatment with environmental conditions hypoxia (200nM $CoCl_2$), acidosis (pH of 5.5), or starvation (1:10 dilution) normalized to growth under normal media. Mean and two replicates shown. Tukey's multiple comparisons test was used; only comparisons to the parental sample within each time period are shown. **H.** Quantification of viability staining after short term or long term treatment with trametinib (15nM), ruxolitinib (20µM), or rapamycin (10µM) normalized to vehicle control (DMSO, 0.025%). Mean and three replicates shown. Tukey's multiple comparisons test was used; only comparisons to the parental sample within each time period are shown. **I.** Left: schematic of experimental design where mixed populations of Parental GFP cells and mCherry, either erLor or erAlec, cells were injected subcutaneously. Both the primary subcutaneous site and lung metastatic site were collected and cells enumerated via FACS. Right: percent of each cell type found in given organ based on FACS analysis after 27 days post injection. Unpaired t-tests shown. **J.** Left: schematic of experimental design where a mixed populations of Parental GFP+ cells and mCherry+, either erLor or erAlec, cells were injected via tail vein. Right: percent of each cell line found in the lungs after 27 days post injection. One-way ANOVA with Dunnett's multiple comparisons test shown.

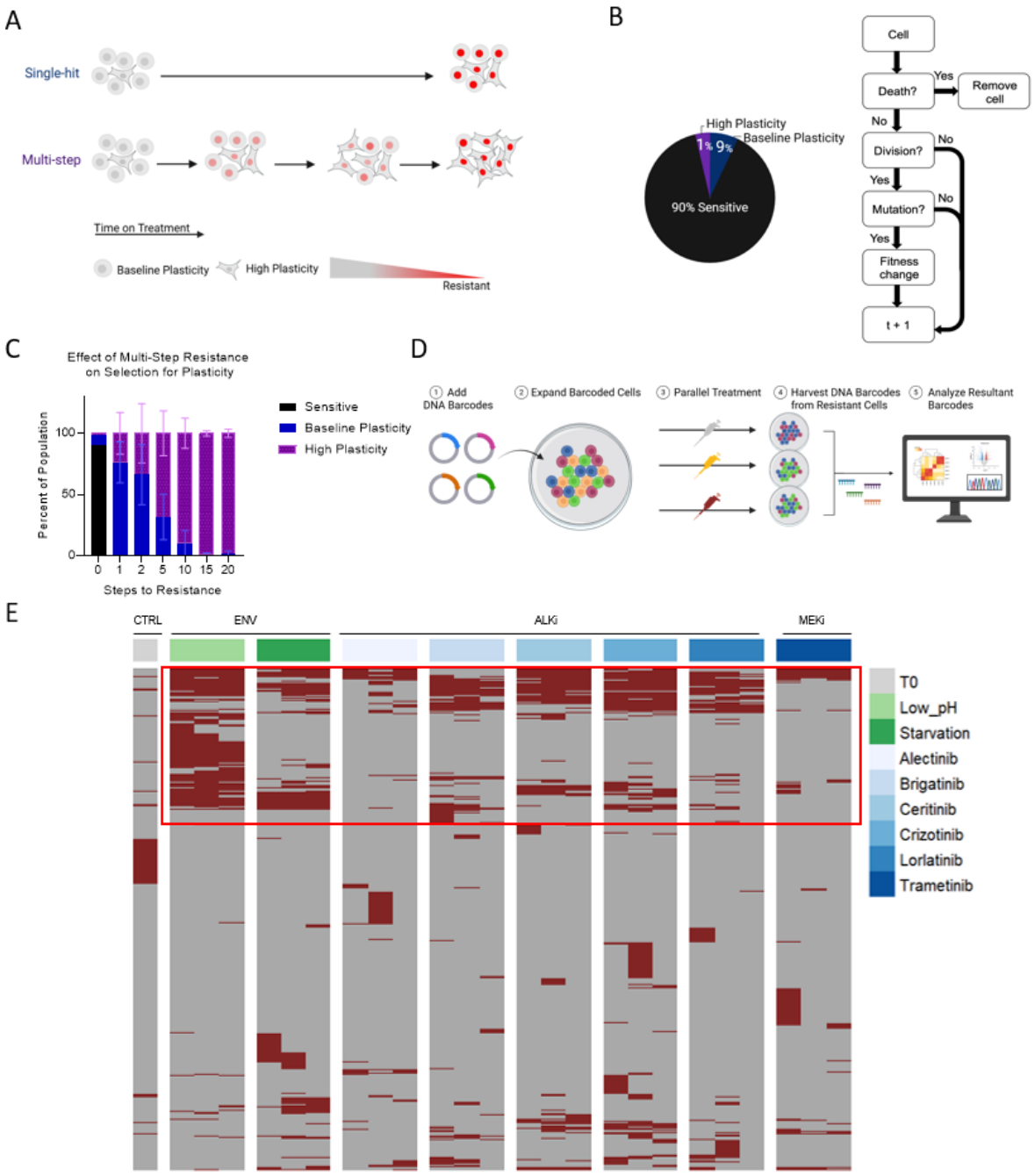

Figure 2. Treatment and exposure to harsh environments drive gradual selection for rare cells with higher adaptability. A. Schemata of hypotheses. **B.** Left: Schematic of initial simulation conditions. Right: schematic of agent-based model (ABM) algorithm. **C**. Cell fraction of each population after 600 timesteps based on the number of steps to resistance modeled in each simulation. Mean ± SD shown of 10 simulations. **D.** Schematic of experimental design for barcode libraries. **E.** Unsupervised hierarchical clustering of barcodes from CloneTracer library in each sample based on presence in given treatment. Each row represents a barcode. Each column represents a replicate of a condition. n= 1 for T0, n=3 for all other arms. CTRL = control, T0= time zero, initial time point; ENV = environmental stressor, ALKi= ALK inhibitor, MEKi= MEK inhibitor. DMSO (0.1%), alectinib (0.5μM) lorlatinib (0.5μM), crizotinib (0.5μM), ceritinib (0.1μM), brigatinib (0.1μM), trametinib (0.1μM), Low_pH pH of 6, starvation 1:5 media:PBS.

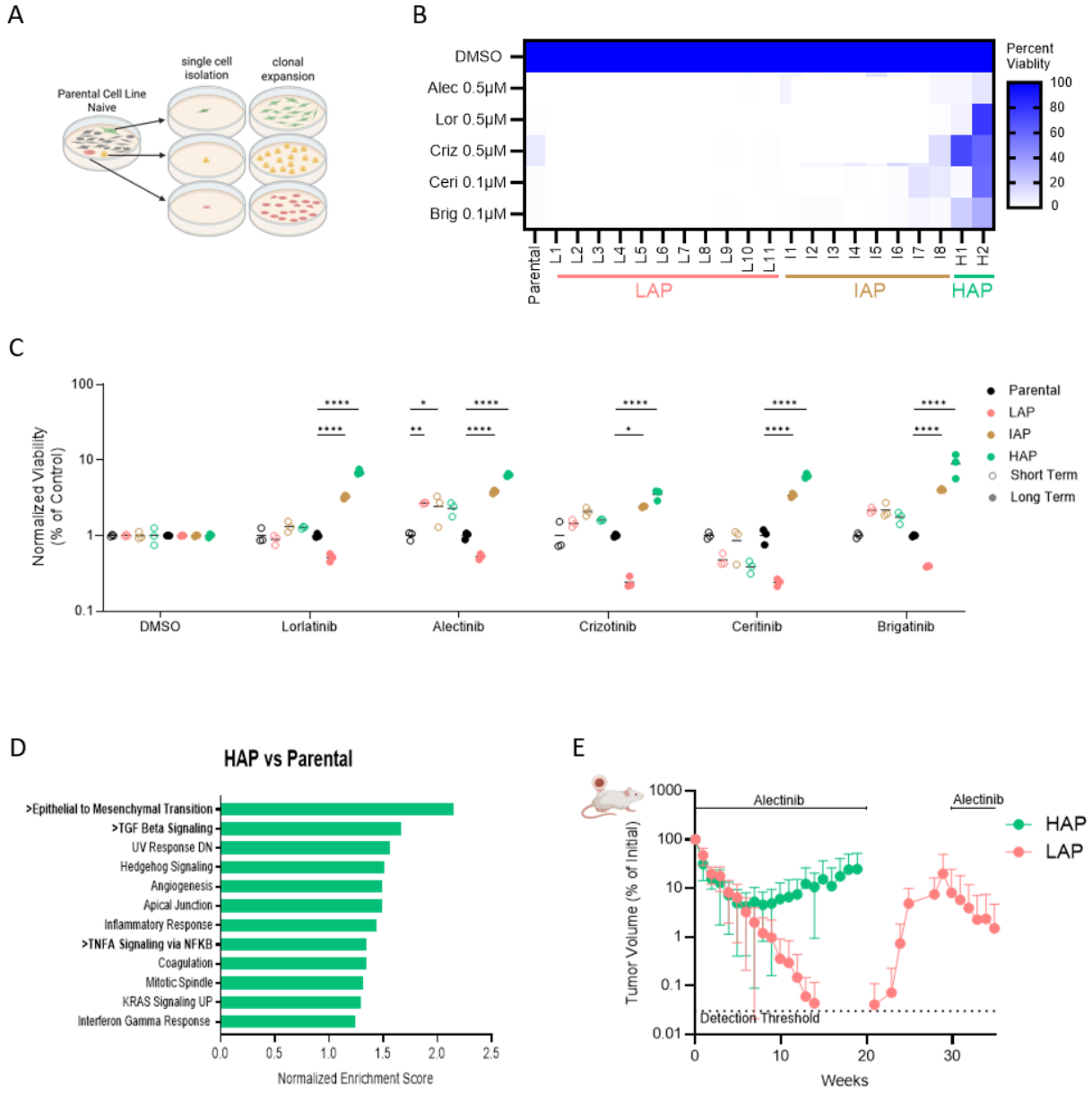

Figure 3. Single-cell-derived clones can be classified into adaptation potentials with distinct functional and molecular profiles. A. Schematic of experimental categorization of single-cell derived clones. **B.** Heatmap representing Image J crystal violet quantification as a percent confluence of each cell line compared to vehicle treatment (DMSO) for up to three months in treatment. Drug treatment displayed as rows, clone number listed as columns for the 21 clones that expanded from single-cell sorting, with final classifications as low, intermediate, or high adaptation-potential. **C.** Cell Titer Glo quantification of representative clones from each category of LAP, IAP, or HAP. Percent viability after 3 days (short term) or 21 days (long term) normalized to growth under vehicle control (DMSO, 0.025%). Mean and three replicates shown. Tukey's multiple comparisons test was used; only comparisons to the parental sample within each time period are shown. **D.** Significantly enriched pathways from Gene Set Enrichment Analysis (GSEA) of hallmark gene sets in HAP versus Parental cells from RNA sequencing. Pathways with ≥1.25 normalized enrichment score (NES) shown. **E.** Volumetric traces of HAP and LAP H3122 xenograft tumors on treatment with 25mg/kg alectinib for 20 weeks, followed by a treatment break for LAP tumors for 9 weeks, followed by re-treatment for LAP tumor-bearing mice for 5 weeks. Mean ± SD shown. P values using mixed effect model in Supplementary Table 1 (n= 8 tumors per group).

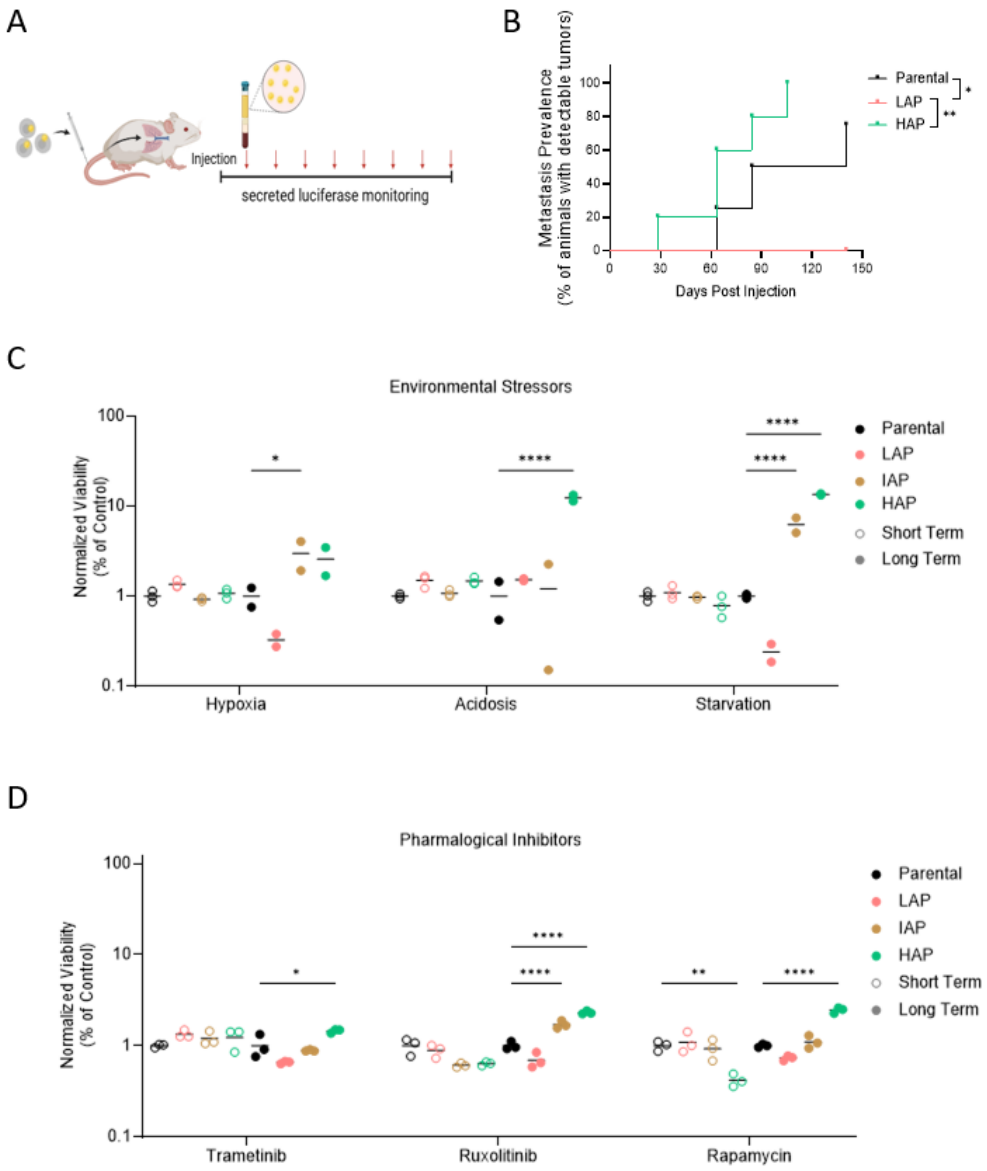

Figure 4. TKI adaptation-potential extends to metastatic potential and multi-stress resistance. **A.** Schematic of metastasis experiment with continuous monitoring via luciferase assay of blood plasma. **B.** Cumulative Incidence plot of percent of animals in each group that developed metastasis, as measured by luciferase activity in plasma. n=5 for LAP and HAP groups, n=4 for Parental group. Logrank (Mantel-Cox) test shown. **C.** *In vitro* quantification of crystal violet viability staining of representative cell lines of Parental, LAP, IAP, or HAP in hypoxia (200nM $CoCl_2$), acidosis (5.5 pH), or starvation (1:5 media:PBS) normalized to growth under normal media after 3 days (short term) or 16 days (long term). Mean and three replicates (short term) or two replicates (long term) shown. Tukey's multiple comparisons test was used; only comparisons to the parental sample within each time period are shown. **D.** *In vitro* quantification of crystal violet viability staining of representative cell lines of Parental, LAP, IAP, HAP, erLor, or erAlec in trametinib (15nM), ruxolitinib (20μM), rapamycin (10μM) normalized to growth under vehicle control (DMSO, 0.025%) after 3 days (short term) or 22 days (long term). Mean and three replicates shown. Tukey's multiple comparisons test was used; only comparisons to the parental sample within each time period are shown.

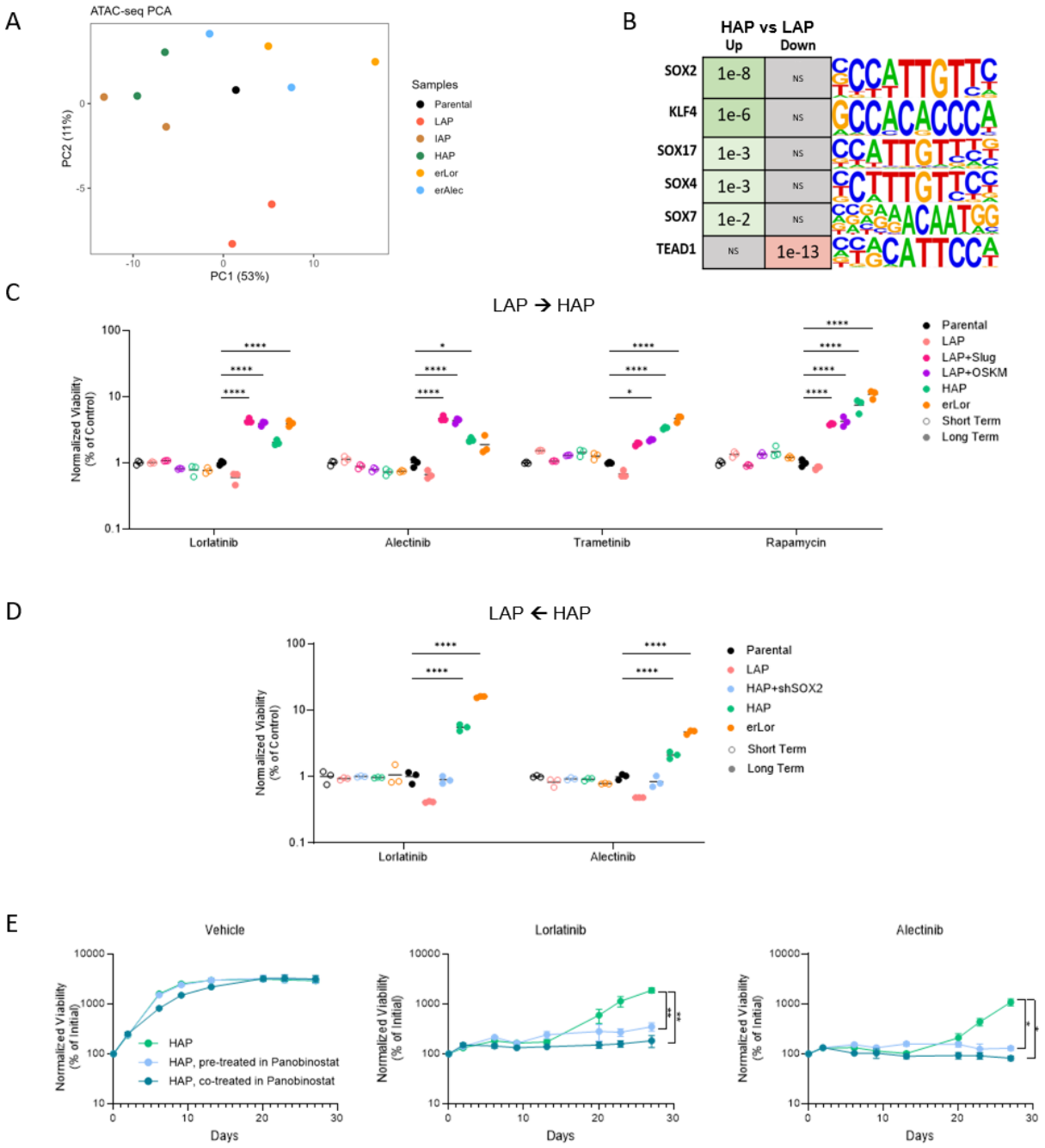

Figure 5. Adaptation-potential can be manipulated. **A.** PCA of top 500 variable genes from bulk ATAC- sequencing. **B.** HOMER known motif enrichment analysis of motifs enriched in HAP cells compared to LAP cells (value in table) in relevant transcription factors. P -value shown in table. NS, not statistically significant. **C.** Quantification of crystal violet viability staining of Parental, LAP, HAP, LAP + Slug or LAP + OSKM cells in lorlatinib (0.5μM), alectinib (0.5μM), trametinib (15nM), or rapamycin (10μM) normalized to growth in vehicle control (DMSO, 0.025%), after 3 days (short term) or 4 weeks (long term). Mean and three replicates shown. Tukey's multiple comparisons test was used; only comparisons to the parental sample within each time period are shown. **D.** Quantification of crystal violet viability staining of Parental, LAP, HAP, HAP + shSOX2, and erLor cells in lorlatinib (0.5μM), or alectinib (0.5μM) normalized to vehicle control (DMSO, 0.025%) after 3 days (short term) or 4 weeks (long term). Mean and three replicates shown. Tukey's multiple comparisons test was used; only comparisons to the parental sample within each time period are shown. **E.** Quantification by live cell imaging of percentage of area covered by cells treated with vehicle (DMSO, 0.025%; left), lorlatinib (0.5μM; middle), or alectinib (0.5μM; right) with pre-treatment of co-treatment with Panobinostat (2nM). 2-way ANOVA with repeated measurements and Tukey's multiple comparison in Supplementary Table 1; comparison to HAP shown.